

Interpretation of edge pedestal rotation measurements in DIII-D

W. M. Stacey¹ and R. J. Groebner²

¹Georgia Institute of Technology, Atlanta, Georgia 30332, USA

²General Atomics, San Diego, California 92186, USA

(Received 30 October 2007; accepted 7 December 2007; published online 25 January 2008)

A novel methodology for inferring experimental toroidal angular momentum transfer rates from measured toroidal rotation velocities and other measured quantities has been developed and applied to analyze rotation measurements in the DIII-D [J. Luxon, *Nucl. Fusion* **42**, 6149 (2002)] edge pedestal. The experimentally inferred values have been compared with predictions based on atomic physics processes and on neoclassical toroidal viscosity. The poloidal rotation velocities have been calculated from poloidal momentum balance using neoclassical parallel viscosity and a novel retention of all terms in the poloidal momentum balance, and compared with measured values in the DIII-D edge pedestal. © 2008 American Institute of Physics. [DOI: 10.1063/1.2830653]

I. INTRODUCTION

There is a long-standing research interest in the steep-gradient edge pedestal region (e.g., Refs. 1–4) of high confinement (H-mode) tokamaks, stimulated at least in part by predictions^{5,6} that, because of the “stiffness” observed in core plasma temperature profiles, the achievable central temperatures and densities in future tokamaks will be sensitive to the values of the temperature and density at the top of the edge pedestal.

We previously have shown^{7,8} that momentum balance determines a requirement on the main ion pressure gradient $L_{pi}^{-1} \equiv -(\partial p_i / \partial r) / p_i = (V_{ri} - V_{pinch,i}) / D_i$, where V_{ri} is the radial particle velocity (which must satisfy the continuity equation), $V_{pinch,i}$ is a collection of terms involving the poloidal and toroidal rotation velocities and other terms (radial and toroidal electric field, beam momentum input), and D_i is a diffusion coefficient type term involving interspecies and viscous momentum transfer frequencies. It was found⁸ that the pinch term (hence the rotation velocities and the radial electric field) dominated the determination of the edge pressure gradient in several DIII-D⁹ shots. Thus, the next question is what causes the structure in the rotation velocity profiles in the edge pedestal (which in turn cause the structure in the density and pressure profiles in the edge pedestal). We note the probable relevance to our investigation of previous investigations of nonmonotonic toroidal rotation velocities observed in the vicinity of steep pressure gradients—at internal transport barriers¹⁰ and in supershots.¹¹

Thus motivated, we have undertaken a study of rotation velocities measured in the DIII-D edge pedestal. Detailed edge profile data that were assembled for the velocity profiles (and density and temperature profiles) in the edge pedestal of two H-mode DIII-D plasmas are described in Sec. II. The formalism used for the interpretation of these data is described in Secs. III–V. The interpretation of the data to infer information on the momentum transfer rates existing in the edge plasma and to compare with predictive calculations of the poloidal rotation velocities are discussed in Sec. VI. Finally, the results are summarized and conclusions are discussed in Sec. VII.

II. ROTATION MEASUREMENTS AND ANALYSIS

The DIII-D charge-exchange recombination (CER) spectroscopy system¹² enables measurements of toroidal and poloidal velocities for the dominant carbon VI impurity species. Edge pedestal rotation profiles and density and temperature profiles averaged over several measurements have been analyzed for three shot/times, employing the formalism presented in subsequent sections. The rotation profile data are discussed in this section, and the density and temperature profiles have been discussed in previous papers.^{13,14}

Discharge 119436 was run in a lower single null divertor (SND) configuration with plasma current $I_p = 1.0$ MA, toroidal field $B_t = 1.6$ T, and average triangularity $\delta = 0.35$. During the time of interest (3.0–3.5 s), the injected beam power P_{beam} was 4.3 MW, the line-averaged density $\langle n_e \rangle$ was about $0.34 \times 10^{20} \text{ m}^{-3}$, the global stored energy W_{MHD} was about 0.55 MJ, and the average edge localized mode (ELM) period was 15.3 ms. Even though the global parameters, such as $\langle n_e \rangle$ and W_{MHD} , were approximately constant during the time of interest, the conditions in the pedestal were constantly changing due to the effect of ELMs. The period 80%–99% between ELMs was chosen for analysis for this shot.

Discharge 98889 was also run in a lower SND configuration with $I_p = 1.2$ MA, toroidal field $B_t = 2.0$ T, and average $\delta = 0.07$. During the time of interest (3.75–4.11 s), P_{beam} was 3.1 MW, $\langle n_e \rangle$ was about $0.40 \times 10^{20} \text{ m}^{-3}$, W_{MHD} was about 0.59 MJ, and the average ELM period was 36.0 ms. Similar to discharge 119436, the maximum electron pressure gradient varied by at least a factor of 2–3 during an ELM cycle, even though the global parameters were roughly constant during the time of interest. The period 40%–60% between ELMs was chosen for analysis for this shot.

Discharge 118897 was also a lower SND configuration with $I_p = 1.4$ MA, toroidal field $B_t = 2.0$ T, and average $\delta = 0.4$. At the time of interest (2.14 s), the plasma was in a well-developed ELM-free H-mode stage with slowly varying parameters $P_{beam} = 2.35$ MW, $\langle n_e \rangle = 7.7 \times 10^{19} \text{ m}^{-3}$, and $W_{MHD} = 0.68$ MJ.

Composite density and temperature profiles, for use in thermal transport calculations, were obtained by fitting data

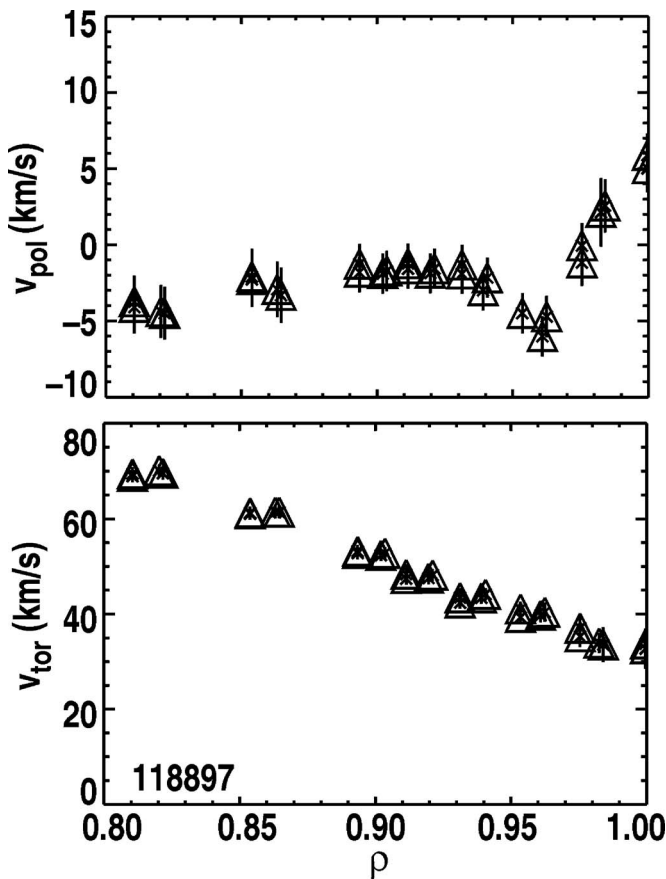


FIG. 1. Measured (CER) toroidal and poloidal rotation velocities for DIII-D shot 118897.

from appropriate time bins during the time of interest in these discharges.^{13,14} For the ELMing shots 119436 and 98889, this process began with the use of an algorithm to determine the start and end time of each ELM, from filtering of a D_α signal. The interval between adjacent ELMs was then subdivided into typically five time intervals for the purpose of binning the data. These intervals were chosen to be some fraction of the time between the ELMs (10%–20%, 20%–40%, 40%–60%, 60%–80%, and 80%–99%). These temperature and density data were then averaged within each bin and fit.

Figures 1 and 2 show measured poloidal and toroidal rotation data, obtained from the C VI 529.05 nm line, for discharges 118897 and 119436, respectively. These measurements are obtained from a system of interleaved vertically viewing and toroidally viewing chords of the CER system.¹² For each pair of vertical and toroidal chords that are separated by less than 0.005 m, knowledge of the chord geometry and the magnetic equilibrium is used to uniquely decompose the line-of-sight velocities to obtain poloidal and toroidal rotation. As plotted, the toroidal rotation is positive when in the direction of plasma current for these discharges, which is also the direction of neutral beam injection; the poloidal rotation is positive when in the direction of the poloidal magnetic field. All data have been mapped to the normalized ρ coordinate, where ρ is the square root of the toroidal flux, with equilibria obtained at the appropriate data acquisition

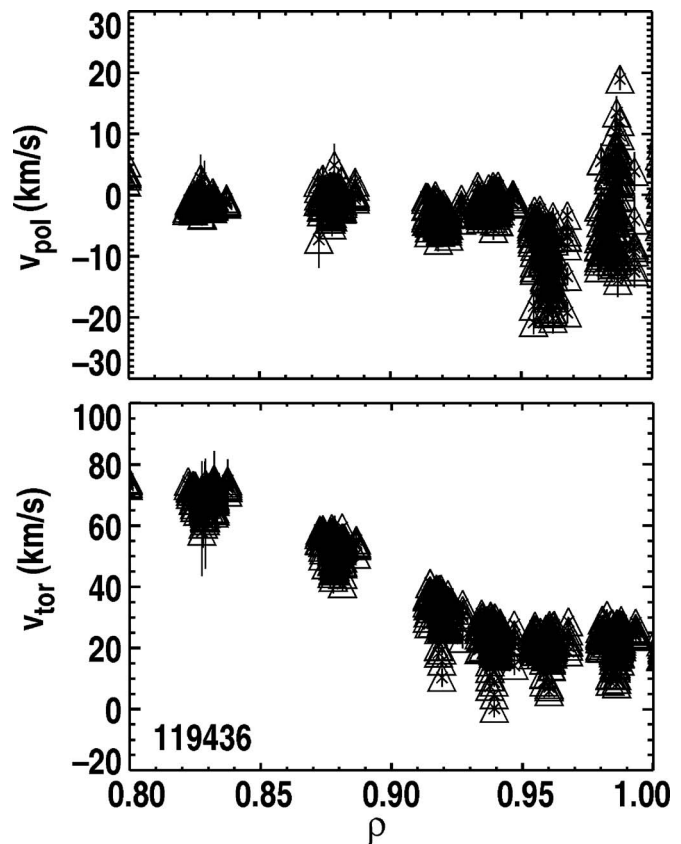


FIG. 2. Measured (CER) toroidal and poloidal rotation velocities for DIII-D shot 119436.

time. Error bars on each measurement, based on photon statistics, are obtained via standard propagation of errors. In some cases, the symbols used in these plots are larger than these error bars.

For discharge 118897, the data were obtained with an averaging time of 5 ms, and four frames of data are shown in the time interval 2120–2170 ms. The neutral beam viewed by the edge CER chords was modulated during this time and background spectra obtained with the beam off were subtracted from spectra with the beam on in order to remove intrinsic emission from C VI in the plasma periphery. For discharge 119436, data were acquired with an averaging time of 0.552 ms. This short time allowed the CER system to capture the time variation of edge parameters within an ELM cycle. The data shown were obtained in the last 20% of the ELM cycle for ELMs occurring in the time window 3000–3400 ms. Beam modulation was not used for this analysis. The ELMs are not perfectly periodic; thus, some of the vertical scatter in the rotation velocities may be due to variations in the length of the various ELM cycles.

The poloidal rotation data for both discharges show the characteristic dip of several km/s in the pedestal (in the vicinity of $\rho=0.95$ – 0.98), which is routinely observed in H-mode discharges in DIII-D. The toroidal rotation decreases with increasing ρ , with some flattening at the plasma edge in discharge 119436. The measurement of the C VI toroidal rotation near the plasma edge should not be considered a measure of the main ion velocity nor should the

impurity poloidal rotation be considered a measure of the main ion poloidal rotation. In TFTR, it was shown that the notch in the C VI toroidal rotation velocity was a result of the large pressure gradient for the main ions.¹¹ Similar physics could be occurring in the H-mode pedestal and forcing the impurity toroidal rotation profile to be different than the main ion rotation. In fact, previous measurements in DIII-D have shown that the impurity and main ion velocities can be significantly different in both the poloidal and toroidal directions.¹⁵ One of the goals of this paper is to examine the coupling between main ion and carbon rotation in the poloidal and toroidal directions.

Great care has been taken to make accurate measurements of rotation velocities down to the level of a few km/s. For instance, a system of neon lamps is used to obtain calibration spectra after every discharge, for the purpose of determining the location on each detector of the unshifted C VI 529.05 nm line.¹⁶ For this purpose, the unshifted wavelength of this line has been determined to required accuracy from opposing measurements of toroidal velocity in tokamak plasmas.¹⁶ In addition, neon spectra data are obtained from within the vessel, by the injection of a neutral beam into neon gas, to correct for a small, high-order aberration in the spectrometers, which causes the location of the wavelength reference to be slightly different for illumination from external lamps as opposed to illumination from within the vessel.

Good knowledge of the geometry of the viewing chords and of the beam geometry is required to accurately remove contributions of toroidal rotation from the vertical chords in order to obtain poloidal rotation. The chord geometry is generally checked with in-vessel measurements both before and at the end of each major campaign in DIII-D. The geometry of the beamlines has been determined from a variety of survey techniques, including thermocouple measurements from the hit spot of the beam on the inner wall. Small errors in the geometry cannot be ruled out, but there is no reason to suspect any problems for the edge measurements presented here. Other possible sources of error include atomic physics effects due to gyromotion and energy-dependent cross-section effects.¹⁷ Correcting for these is a complex process and the corrections are not yet available in the codes used for edge rotation analysis at DIII-D. However, these effects are small at low temperature and are not expected to be a significant problem.

Other systematic errors could arise from the inability to adequately remove the contribution of the intrinsic edge C VI 529.05 nm light to the CER spectra. For discharge 118897, the beam modulation technique mostly eliminates this problem. In cases where the modulation technique is not available, such as for discharge 119436, it is rarely possible to separate the intrinsic emission from the CER emission in the pedestal via the spectral fitting process. Thus, the results can contain some effect from the intrinsic emission, which might not have the same rotation as the CER emission. Generally, the CER line is quite strong relative to the intrinsic emission except for measurements at the separatrix and on the open field lines. Thus, this effect is not generally a significant problem.

In summary, the approach here is to obtain multiple ro-

tation profiles for nominally identical plasma conditions. The scatter in the results gives the best available estimate of the uncertainties in the measurements. However, there may remain small systematic errors in mapping data to magnetic equilibria. For the CER data, measured at the outer mid-plane, the plausible magnitude of these errors is no more than about 2% of the normalized toroidal flux. Along the vertical chord of the Thomson scattering system, the plausible errors are 3%–4% of the normalized toroidal flux. However, it is believed that the procedure used to adjust the location of the Thomson data to the separatrix, described, e.g., in Ref. 14, eliminates most of the systematic error in mapping for the Thomson system. The potential mapping errors for these two systems imply that there could be systematic errors in quantities that require data from both systems; e.g., the experimental main ion pressure gradient and the collisional ion-electron energy exchange term in the energy flux calculation.

An integrated modeling code¹⁸ was used to supplement the experimental data. This code (i) calculated particle and power balances on the core plasma to determine the net particle and heat outfluxes from the core into the scrape-off layer (SOL), calculated using measured energy confinement times and particle confinements times from “die-away” measurements, which were input to (ii) an extended two-point divertor plasma model (with radiation and atomic physics) that calculated densities and temperatures in the SOL and divertor and the ion flux incident on the divertor plate, which (iii) was recycled as neutral atoms and molecules that were transported through the two-dimensional divertor region across the separatrix to fuel the core plasma. For the ELMing shots, this code calculated “steady-state” (averaged over ELMs) heat and particle outfluxes into the SOL (based on matching experimental line-averaged density). This steady-state particle outflux was used to calculate a recycling neutral source at the divertor plate, which was held constant over the ELM cycle (i.e., averaged over ELMs). However, a time-dependent neutral influx into the pedestal regions was then calculated using this “ELM-averaged” recycling source and the time-dependent experimental edge pedestal density and temperature profiles discussed above, resulting in different neutral influxes at different times in the interval between ELMs.

III. PARTICLE AND MOMENTUM BALANCE

The interpretation of the rotation measurements in this paper is based on particle and momentum balance. A fluid model for the edge plasma was employed, with kinetic effects included via constitutive relations for the collisional friction and viscosity. The basic equations are first written for a general ion species j in the presence of other ion species k , which interact collisionally (with a sum over k implied). Subsequently, the formalism is reduced to two species: a main ion species and an impurity species.

The particle continuity equation for ion species j is

$$\nabla \cdot \Gamma_j \equiv \nabla \cdot n_j \mathbf{v}_j = S_j - \frac{\partial n_j}{\partial t}, \quad (1)$$

where $S_j = n_e(r, \theta) n_{j0}(r, \theta) \langle \sigma v \rangle_{\text{ion}} \equiv n_e(r, \theta) \nu_{\text{ion}}(r, \theta)$ is the ionization source rate of ion species j and n_{j0} is the local concentration of neutrals of species j . The time-independent momentum balance equation for ion species j is

$$\begin{aligned} \nabla \cdot (n_j m_j \mathbf{v}_j \mathbf{v}_j) + \nabla p_j + \nabla \cdot \boldsymbol{\pi}_j \\ = n_j e_j (\mathbf{v}_j \times \mathbf{B}) + n_j e_j \mathbf{E} + \mathbf{F}_j + \mathbf{M}_j - n_j m_j \nu_{\text{el,cx},j}^j \mathbf{v}_j \\ - \frac{\partial (n_j m_j \mathbf{v}_j)}{\partial t}, \end{aligned} \quad (2)$$

where p_j is the pressure, $\boldsymbol{\pi}_j$ represents the viscous momentum flux, \mathbf{E} represents the electric field, $\mathbf{F}_j = -n_j m_j \nu_{jk}(\mathbf{v}_j - \mathbf{v}_k)$ represents the interspecies collisional friction, \mathbf{M}_j represents the external momentum input rate (e.g., due to neutral beams), the next-to-last term represents the momentum loss rate due to elastic scattering and charge exchange with neutrals of all ion species k $\{\nu_{\text{el,cx},j} = \sum_k n_{k0} [(\sigma v)_{\text{el}} + \langle \sigma v \rangle_{\text{cx}}]_{jk}\}$, and as usual (n_j, m_j, e_j, v_j) denote particle density, mass, charge, and velocity of species j , respectively.

In the following sections, we will use these equations in two different ways. First, we will formally solve these equations for the rotation velocities, presuming the use of measured data to evaluate the various “coefficients” arising in various theoretical prescriptions for the friction, viscosity, etc., and make the usual type of comparison of the calculated rotation velocities with the experimental ones. Second, we will “solve these equations backwards” for the composite momentum transport rate (due to the viscous, inertial, and atomic physics mechanisms), which is necessary to produce the measured rotation velocities by using the measured rotation velocities (and density and temperature) profiles as input.

IV. TOROIDAL ROTATION

Toroidal rotation is governed by the flux surface averaged (FSA) toroidal component of the angular momentum balance equation. The toroidal angular momentum balance equations follows from Eq. (2) by multiplication by the major radius.

One of the purposes of this paper is to use the above equations to interpret measured velocity profiles to extract information about the underlying momentum transport rates. For this purpose, it is useful to rewrite these equations in terms of angular momentum transport rates $R n_j m_j \nu_{xj} v_{\phi j}$ associated with process x . The quantity ν_{xj} is referred to as the angular momentum transfer frequency. Expressions for these angular momentum transfer frequencies can be derived from different theoretical models for the various momentum transport mechanisms, as discussed immediately below and in Ref. 19, and evaluated using experimental data to obtain theoretical values for the angular momentum transfer frequencies. In order to obtain experimental values for angular momentum transfer frequencies for comparison, the rewritten toroidal angular momentum balance equations can be solved for the value of the composite angular momentum transfer

frequency that is required to yield the measured toroidal rotation velocity, using experimental data to evaluate the various terms in the equation.

It is shown elsewhere¹⁹ that the flux surface average neoclassical viscous toroidal torque can be written in the form

$$\langle R^2 \nabla \phi \cdot \nabla \cdot \Pi_j \rangle = R n_j m_j \nu_{\text{visc},j} v_{\phi j} \quad (3)$$

and that the inertial, or convective torque can be similarly written

$$\langle R^2 \nabla \phi \cdot \nabla \cdot (n_j m_j \mathbf{v}_j \mathbf{v}_j) \rangle = R n_j m_j \nu_{\text{inert},j} v_{\phi j} + R n_j m_j \nu_{\text{ion},j} v_{\phi j}, \quad (4)$$

where the $\nu_{\text{visc},j}$ and $\nu_{\text{inert},j}$ are angular momentum transfer frequencies defined in terms of viscosity coefficients and/or radial and poloidal gradients of the density, temperature, and rotation velocities. Anomalous viscosity is usually modeled with the same mathematical structure as the neoclassical perpendicular viscosity but with an enhanced viscosity coefficient, so that anomalous viscosity can also be recast in the form of Eq. (3). For our purposes in this paper, the radial gradients that enter the theoretical definitions of these angular momentum transfer frequencies can be evaluated from measured density, temperature, and rotation velocity profiles. The atomic physics angular momentum loss due to charge-exchange and elastic scattering of recycling or beam injected neutrals has the same $R n_j m_j \nu_{\text{el,cx},j} v_{\phi j}$ form. [The $R n_j m_j \nu_{\text{ion},j} v_{\phi j}$ term in Eq. (4) arises from use of Eq. (1) in evaluating the term on the left.]

Thus, the FSA toroidal angular momentum balance equation for plasma species j can quite generally be written⁸

$$n_j m_j [\nu_{jk}(\mathbf{v}_{\phi j} - \mathbf{v}_{\phi k}) + \nu_{dj} v_{\phi j}] = n_j e_j E_{\phi}^A + e_j B_{\theta} \Gamma_{rj} + M_{\phi j}, \quad (5)$$

where ν_{dj} represents the total toroidal angular momentum transfer frequency due to neoclassical and anomalous viscosity (or torques), convection, atomic physics, and other processes (e.g., field ripple) that can be written in the $R n_j m_j \nu_{xj} v_{\phi j}$ form, ν_{jk} is the interspecies collision frequency (a sum over all other species $k \neq j$ is implied), E_{ϕ}^A is the electromagnetically induced toroidal electric field, $\Gamma_{rj} \equiv n_j v_{rj}$ is the radial particle flux determined by solution of the continuity equation (1), and $M_{\phi j}$ is the toroidal component of the momentum input (e.g., by neutral beams).

An “anomalous torque” can be represented in the above equations either by considering the input torque to consist of neutral beam plus anomalous torques ($RM_{\phi} = RM_{\phi,\text{nb}} + RM_{\phi,\text{anom}}$), or by considering the cross-field angular momentum transport processes to include neoclassical, inertial, atomic physics, and anomalous processes ($\nu_{dj} = \nu_{dj}^{\text{visc}} + \nu_{dj}^{\text{inert}} + \nu_{dj}^{\text{atom}} + \nu_{dj}^{\text{anom}}$). We use this latter option in this paper.

A. Formal solution of the toroidal rotation equations

The quantities on the right side of Eq. (5) are generally either known, measured experimentally, or can be determined by solving the continuity equation, and ν_{jk} can be calculated if the density and temperature are known experimentally. Thus, if the ν_{dj} are known (e.g., evaluated from theoretical expressions such as those given above using the measured density and temperature profiles and rotation ve-

locity gradient scale lengths), then Eq. (5) can be solved for the toroidal rotation velocities. For a “two-ion-species” plasma, Eq. (5) can be summed over both ion species and electrons, and charge neutrality and ambipolarity can be invoked to obtain

$$v_{\phi j} = -\frac{n_k m_k v_{dk}}{n_j m_j v_{dj}} v_{\phi k} + \frac{M_\phi}{n_j m_j v_{dj}}, \quad (6)$$

where M_ϕ is the total toroidal momentum input to all species. A similar equation obtains for the other ion species k , but with the j and k subscripts interchanged.

Equation (6) may offer an explanation for the observation in DIII-D that the measured carbon (species k) rotation velocity is sometimes in the opposite direction from the momentum input in the plasma edge. The beam input in the edge is small and the unmeasured main ion (species j) velocity (which carries most of the angular momentum) could be in the opposite direction from the measured carbon velocity (species k).

Using Eq. (6) to eliminate $v_{\phi j}$ from Eq. (5) yields

$$v_{\phi k} = \frac{[v_{dj} M_{\phi k} + v_{jk} M_\phi - v_{dj} (n_j e_j E_\phi^A + e_j B_\theta \Gamma_{rj})]}{[v_{jk} (n_j m_j v_{dj} + n_k m_k v_{dk}) + v_{dj} n_k m_k v_{dk}]} \quad (7)$$

(and a similar equation with “ j ” and “ k ” subscripts interchanged). The first term in the numerator represents the external momentum input directly to species k and the second term is related to the external momentum input transferred collisionally to species k , while the last two terms represent internal torques due to the induced toroidal electric field and the radial particle flux. The coordinate system was chosen such that the positive ϕ direction is in the direction of the plasma current, so that E_ϕ^A and B_θ are positive.

Equation (7) indicates that in the absence of an external momentum input ($M_\phi=0$) there will be a rotation of species k in the direction counter to the plasma current when $v_{dj} > 0$ (corresponding to radially outward angular momentum transport or momentum loss from the flux surface) and $\Gamma_{rj} > 0$ (outward) or small. (The contribution to v_{dj} from charge-exchange is positive by definition, we consistently calculate $v_{dj} > 0$ from neoclassical viscous and inertial terms, and we consistently find $\Gamma_{rj} > 0$ and increasing with radius in the edge pedestal because of the ionization of recycling neutrals.) Achievement of co-rotation of carbon (species k) in the absence of net beam momentum input, as has been observed in H-mode plasmas in C-Mod²⁰ and DIII-D,²¹ would require an anomalous external momentum input ($M_\phi^{\text{anom}} > 0$), the magnitude of which could be inferred from Eq. (7) if the internal momentum transfer frequencies for both species were known.

B. Inference of experimental angular momentum transfer frequency

A novel approach that we pursue in this paper is to use the measured rotation velocities as input in “solving the equations backwards” to infer the local momentum transport frequency from the toroidal angular momentum equation. Equation (5) for each species can be readily rearranged to yield (for the two-ion-species model) a requirement on the

composite angular momentum transport frequency for all mechanisms (classical and anomalous viscosity, inertial, atomic physics, etc.) that must be satisfied in order to produce the measured rotation velocities

$$v_{dj} = v_{jk} \left[\frac{n_j e_j E_\phi^A + e_j B_\theta \Gamma_{rj} + M_{\phi j}}{n_j m_j v_{jk} v_{\phi j}} - \left(1 - \frac{v_{\phi k}}{v_{\phi j}} \right) \right] \quad (8)$$

(and a similar expression with the “ j ” and “ k ” subscripts interchanged). All quantities on the right except the rotation velocities can be readily determined from measurements and solving the continuity equation. Thus, if the toroidal rotation velocities for both ion species are also measured, the momentum transfer frequencies for both species can be determined from Eq. (8) (plus the same equation with j and k interchanged).

An immediate problem arises because it is not presently possible to measure the rotation velocity for deuterium, the usual main ion species. It is tempting to try using the radial momentum balance equations for both species,¹⁵

$$E_r/B_\theta = v_{\phi j} - f_p^{-1} v_{\theta j} + P'_j, \quad (9)$$

where $f_p = B_\theta/B_\phi$ and $P'_j = (\partial p_j / \partial r) / (n_j e_j B_\theta)$, to relate $v_{\phi j}$ and $v_{\phi k}$

$$(v_{\phi j} - v_{\phi k}) = f_p^{-1} (v_{\theta j} - v_{\theta k}) - (P'_j - P'_k), \quad (10)$$

but this introduces another unmeasurable quantity; i.e., the deuterium poloidal velocity. Thus, an unambiguous determination of the radial transfer rates of toroidal angular momentum requires a measurement of the toroidal rotation velocities of both the main ion and a dominant impurity ion species (e.g., a helium plasma with carbon impurity, such as in Ref. 22).

To get around this problem, we use a perturbation analysis of the above toroidal momentum balance equations for a two-species [deuterium (j); carbon impurity (k)] plasma to first obtain an estimate of the difference in the deuterium and carbon toroidal velocities. This difference can be added to the measured carbon velocity to obtain what we will call an “experimental” deuterium velocity. The measured carbon velocity and the experimental deuterium velocity can then be used to solve the toroidal momentum balance equations backwards for the experimental angular momentum transfer frequencies (arising from all processes including anomalous ones) that are required in order for the toroidal momentum balance equations to yield the two experimental toroidal velocities.

First, the toroidal momentum balance Eq. (5) for the two species are added to eliminate the friction terms and used to define an effective momentum transfer frequency

$$\nu_d^{\text{eff}} \equiv \frac{n_j n_j \nu_{dj} + n_k m_k \nu_{dk}}{n_j m_j + n_k m_k} = \frac{(n_j e_j E_\phi^A + e_j B_\theta \Gamma_{rj} + M_{\phi j}) + (n_k e_k E_\phi^A + e_k B_\theta \Gamma_{rk} + M_{\phi k}) - \{n_j m_j \nu_{dj} (\mathbf{v}_{\phi j} - \mathbf{v}_{\phi k})\}}{(n_j m_j + n_k m_k) \nu_{\phi k}}. \quad (11)$$

The $\{ \}$ term involving the difference in toroidal velocities is set to zero to obtain a zeroth-order approximation of the effective momentum transport frequency ν_d^0 ,

$$\nu_d^0 = \frac{(n_j e_j E_\phi^A + e_j B_\theta \Gamma_{rj} + M_{\phi j}) + (n_k e_k E_\phi^A + e_k B_\theta \Gamma_{rk} + M_{\phi k})}{(n_j m_j + n_k m_k) \nu_{\phi k}^{\text{exp}}}, \quad (12)$$

which is used, along with the measured carbon toroidal velocity $\nu_{\phi k}^{\text{exp}}$ in Eq. (5) for the deuterium j species, to obtain a zeroth-order approximation for the deuterium-carbon velocity difference

$$(\mathbf{v}_{\phi j} - \mathbf{v}_{\phi k})_0 = \frac{(n_j e_j E_\phi^A + e_j B_\theta \Gamma_{rj} + M_{\phi j}) - n_j m_j \nu_d^0 \nu_{\phi k}^{\text{exp}}}{n_j m_j (\mathbf{v}_{jk} + \mathbf{v}_d^0)}, \quad (13)$$

which in turn is used in Eq. (5) for the carbon impurity k species to solve for the carbon momentum transport frequency

$$\nu_{dk} = \frac{(n_k e_k E_\phi^A + e_k B_\theta \Gamma_{rk} + M_{\phi k}) + n_k m_k \nu_{kj} (\mathbf{v}_{\phi j} - \mathbf{v}_{\phi k})_0}{n_k m_k \nu_{\phi k}^{\text{exp}}}. \quad (14)$$

The deuterium momentum transfer frequency is then calculated from the definition of Eq. (11) using $\nu_d^{\text{eff}} \approx \nu_d^0$, which yields $\nu_{dj} \approx \nu_d^0$.

When we speak subsequently of the experimentally inferred angular momentum transport frequencies, we are referring to the quantities calculated from experimental data using Eqs. (12)–(14), with $\nu_{dj} = \nu_d^0$. We will test (and confirm) the assumption that the difference in toroidal velocities between the main ion and principal carbon impurity ion is small, thus confirming the validity of a perturbation approach.

V. POLOIDAL ROTATION

Poloidal rotation is governed by the poloidal component of the momentum balance equation

$$\begin{aligned} n_j m_j [(\mathbf{v}_j \cdot \nabla) \mathbf{v}_j]_\theta + [\nabla \cdot \Pi_j]_\theta + \frac{1}{r} \frac{\partial p_j}{\partial \theta} - M_{\theta j} \\ + n_j m_j \nu_{jk} (\mathbf{v}_{\theta j} - \mathbf{v}_{\theta k}) + n_j e_j (v_{rj} B_\phi - E_\theta) \\ + n_j m_j \nu_{\text{ion},j} \mathbf{v}_{\theta j} + n_j m_j \nu_{\text{el},\text{cx},j} \mathbf{v}_{\theta j} = 0, \end{aligned} \quad (15)$$

where the poloidal component of the inertial term is¹⁹

$$\begin{aligned} n_j m_j [(\mathbf{v}_j \cdot \nabla) \mathbf{v}_j]_\theta \\ = n_j m_j \left[v_{rj} \frac{\partial v_{\theta j}}{\partial r} + \frac{v_{rj} v_{\theta j}}{r} + \frac{1}{2} \frac{1}{r} \frac{\partial v_{\theta j}^2}{\partial \theta} + \frac{v_{\phi j}^2}{R} \sin \theta \right] \end{aligned} \quad (16)$$

and the poloidal component of the parallel viscous force will

be written using the neoclassical representations discussed in the Appendix. We represent the poloidal density, velocity, and potential asymmetries with a low-order Fourier expansion

$$n_j(r, \theta) \approx n_j^0(r) [1 + n_j^c \cos \theta + n_j^s \sin \theta]. \quad (17)$$

This results in a set of FSA (flux surface averaged) poloidal momentum balance equations, one for each ion species

$$\begin{aligned} \hat{v}_{\theta j} \left[-q \hat{v}_{\phi j} \varepsilon (\tilde{n}_j^s + \tilde{\Phi}^s) + q^2 f_{jp} \left(1 + \tilde{\Phi}^c + \frac{2}{3} \tilde{n}_j^c \right) + f_p \nu_{jk}^* \right. \\ \left. + f_p \nu_{\text{atom},j}^* \right] - \hat{v}_{\theta k} \nu_{jk}^* \sqrt{\frac{m_i}{m_k}} f_p \\ = -\hat{v}_{rj} - q \varepsilon \frac{1}{4} \tilde{n}_j^s - q \varepsilon \hat{\Phi}_j \left[\frac{1}{4} (\tilde{\Phi}^s) \right] + q^2 f_{jp} (\hat{v}_{\phi j} + \hat{P}_j') \tilde{\Phi}^c \\ - q \varepsilon \hat{v}_{\phi j} \left[(\hat{v}_{\phi j} + \hat{P}_j') \tilde{\Phi}^s + \frac{1}{2} \hat{v}_{\phi j} \tilde{n}_j^s \right], \end{aligned} \quad (18)$$

where $\varepsilon = r/R$, $\hat{v}_{\theta j} = v_{\theta j}/f_p u_{\text{th},j}$, $\hat{v}_{\phi j} = v_{\phi j}/u_{\text{th},j}$, $\hat{P}_j' = P_j'/u_{\text{th},j}$, $\tilde{n}_j^{s,c} = n_j^{s,c}/\varepsilon$, $f_p \equiv B_\theta/B_\phi$, and $\hat{\Phi}_j \equiv e_j \Phi^0/T_j$. The atomic physics momentum transfer frequency $\nu_{\text{atom},j} = \nu_{\text{el},\text{cx}} + \nu_{\text{ion}}$ consists of a momentum loss rate due to the charge-exchange and elastic scattering term that enters the momentum balance directly plus an ionization term that enters via the inertia terms analogous to Eq. (4). The electron momentum balance can be solved for $\tilde{\Phi}^{c/s} \equiv \Phi^{c/s}/\varepsilon = n_e^{c/s}/\varepsilon (e \Phi^0/T_e)$, which represents the poloidal asymmetry in the electrostatic potential. The FSA of the electrostatic potential, i.e., Φ^0 , is conventionally determined by integrating the radial electric field radially inward from the first grounded (in contact with the vessel) field line. The friction terms are identified by $\nu_{jk}^* = \nu_{jk} q R / u_{\text{th},j}$, and the viscosity terms resulting from the use of the Shaing–Sigmar²³ expression $\eta_{0j} = n_j m_j u_{\text{th},j} q R f_j (\nu_{jj}^*)$ are identified by $f_j = \varepsilon^{-3/2} \nu_{jj}^* / (1 + \varepsilon^{-3/2} \nu_{jj}^* (1 + \nu_{jj}^*))$, both in Eq. (18) and in Eqs. (20) and (21) below.

The term

$$\hat{v}_{rj} \equiv \frac{e_j B_\phi}{m_j u_{\text{th},j}} \frac{q R}{u_{\text{th},j}} v_{rj} + \frac{f_j q^2 B_\phi}{u_{\text{th},j}} \frac{K^j T_j L_{Ti}^{-1}}{e_j B^2} \quad (19)$$

represents the poloidal rotation driving forces from the $\mathbf{V} \times \mathbf{B}$ force and the heat flux in the parallel viscous force.

The $\tilde{n}_j^{s,c} = n_j^{s,c}/\varepsilon$ represent the poloidally asymmetric density components, which can be obtained by solving the equations resulting from taking the $\sin \theta$ and $\cos \theta$ FSA moments of the poloidal momentum balance equations²⁴

$$\begin{aligned}
& \tilde{n}_j^s \left[-\frac{1}{3} \frac{q^2}{\varepsilon} f_j f_p \hat{v}_{\theta j} + \frac{1}{2} \varepsilon \hat{v}_{rj} - \frac{1}{2} \varepsilon f_p \sum_{k \neq j} \nu_{jk}^* \hat{v}_{\theta k} \sqrt{\frac{m_j}{m_k}} + \frac{1}{2} q \nu_{\text{atom},j}^* f_p \hat{v}_{\theta j} \right] + \tilde{n}_j^c \left[\frac{1}{2} q f_p^2 \hat{v}_{\theta j}^2 - \frac{1}{4} q + \frac{1}{2} q \nu_{\text{el},\text{cx},j}^* \nu_{\text{ion},j}^* \right] \\
& = -\frac{1}{2} \varepsilon f_p \sum_{k \neq j} \nu_{jk}^* \hat{v}_{\theta j} \tilde{n}_k^s - \frac{1}{4} q \Phi_j [-\tilde{\Phi}^c] + \frac{q^2}{\varepsilon} f_j f_p \left[\frac{1}{2} (\hat{v}_{\theta j} - \hat{v}_{\phi j} - \hat{p}_j') \tilde{\Phi}^s - \frac{1}{2} q f_p^2 \hat{v}_{\theta j}^2 - \frac{1}{2} q \hat{v}_{\phi j}^2 - \frac{1}{2} q \nu_{\text{el},\text{cx},j}^* [f_p \hat{v}_{\theta j} \tilde{n}_{oj}^s + \nu_{\text{ion},j}^* \tilde{n}_{oj}^c] \right. \\
& \quad \left. - q \nu_{\text{ion},j}^* f_p \left[\frac{1}{2} \hat{v}_{\theta j} \left\{ \tilde{n}_{oj}^s \left(1 + \frac{n_e^0}{n_j^0} \right) + \frac{n_e^0}{n_j^0} \tilde{n}_e^s \right\} + \frac{1}{3} \frac{q}{\varepsilon} f_j \frac{n_e^0}{n_j^0} (\tilde{n}_e^c + \tilde{n}_{oj}^c) \right] \right] \quad (20)
\end{aligned}$$

and

$$\begin{aligned}
& \tilde{n}_j^c \left[-\frac{1}{3} \frac{q^2}{\varepsilon} f_j f_p \hat{v}_{\theta j} + \frac{1}{2} \varepsilon \hat{v}_{rj} - \frac{1}{2} \varepsilon f_p \sum_{k \neq j} \nu_{jk}^* \hat{v}_{\theta k} \sqrt{\frac{m_j}{m_k}} + \frac{1}{2} q \nu_{\text{atom},j}^* f_p \hat{v}_{\theta j} \right] + \tilde{n}_j^s \left[-\frac{1}{2} q f_p^2 \hat{v}_{\theta j}^2 + \frac{1}{4} q - \frac{1}{2} q \nu_{\text{el},\text{cx},j}^* \nu_{\text{ion},j}^* \right] \\
& = -\sum_{k \neq j} \tilde{n}_k^c \left[\frac{1}{2} \varepsilon f_p \nu_{jk}^* \hat{v}_{\theta j} \right] - \frac{1}{4} q \Phi_j [\tilde{\Phi}^s] + \frac{q^2}{\varepsilon} f_j f_p \left[\frac{1}{2} \{ (1 + \tilde{\Phi}^c) \hat{v}_{\theta j} - (\hat{v}_{\phi j} - \hat{p}_j') \tilde{\Phi}^c \} - q \hat{v}_{\phi j}^2 \left[\frac{1}{4} \varepsilon \{ \tilde{v}_{\phi j} \tilde{v}_{\phi j} + \tilde{n}_j^c \tilde{v}_{\phi j} + \tilde{n}_j^s \tilde{v}_{\phi j} \} \right] \right. \\
& \quad \left. - \frac{1}{2} q \nu_{\text{el},\text{cx},j}^* [f_p \hat{v}_{\theta j} \tilde{n}_{oj}^c - \nu_{\text{ion},j}^* \tilde{n}_{oj}^s] - q f_p \nu_{\text{ion},j}^* \left[\frac{1}{2} \hat{v}_{\theta j} \left\{ \tilde{n}_{oj}^c \left(1 + \frac{n_e^0}{n_j^0} \right) + \frac{n_e^0}{n_j^0} \tilde{n}_e^c \right\} + \frac{1}{3} \frac{q}{\varepsilon} f_j \frac{n_e^0}{n_j^0} (\tilde{n}_e^s + \tilde{n}_{oj}^s) \right] \right]. \quad (21)
\end{aligned}$$

Diverse edge phenomena are represented in the above equations. Atomic physics effects are explicitly indicated by the ν_{ion}^* , $\nu_{\text{el},\text{cx}}^*$, $\nu_{\text{atom}}^* = \nu_{\text{ion}}^* + \nu_{\text{el},\text{cx}}^*$ terms. The ionization of recycling neutrals also causes the deuterium ν_r to increase rapidly with radius just inside the separatrix, because $\Gamma = n\nu_r$ must increase with radius to satisfy the continuity equation, while n is decreasing rapidly in the same edge pedestal region. A poloidal electrostatic field is created in response to the density asymmetries in satisfaction of the Maxwell–Boltzmann constraint (electron poloidal momentum balance). We find that these effects, which are not included in most poloidal rotation calculations, are important in the calculations to be discussed later.

In order to provide physical insight, we simplify the above equations. If we neglect the poloidal asymmetries in density, rotation velocity, etc. [but retain the poloidal asymmetry in magnetic field $B = B_0/(1 + \varepsilon \cos \theta)$ and major radius $R = R_0(1 + \varepsilon \cos \theta)$ that has been used above], which reduces the inertial term in the poloidal momentum balance to the $\nu_{\text{ion},j}$ term, the set of Eqs. (18) reduces to the set

$$\begin{aligned}
& \left[\frac{q u_{\text{th},j} f_j}{R} + \nu_{jk} + \nu_{\text{atom},j} \right] \nu_{\theta j} - \nu_{jk} \nu_{\theta k} \\
& = -\frac{e_j \nu_{rj} B_\phi}{m_j} - \frac{1}{3} \frac{u_{\text{th},j} f_j q B_\phi K^j T_j L_{Tj}^{-1}}{R e_j B^2}, \quad (22)
\end{aligned}$$

which clearly displays the roles of radial particle flows and radial temperature derivatives in driving poloidal velocity and the roles of viscosity, friction, ionization, and charge-exchange of nonrotating neutrals in damping the rotation. Note that in neglecting the poloidal asymmetries, we have also perforce neglected the poloidal electric field in writing Eq. (22).

If the viscosity function f_j is known for each species [e.g., $f_j = \varepsilon^{-3/2} \nu_{jj}^*/(1 + \varepsilon^{-3/2} \nu_{jj}^*)(1 + \nu_{jj}^*)$], the nonlinear set (pair

for two species) of Eqs. (18)–(21) or (22) can be solved numerically for the poloidal rotation velocities.

A. Backward solution for effective viscosity function f_{eff}

If both the carbon and deuterium poloidal and toroidal rotation velocities could be measured, then Eqs. (18) or (22) could be “solved backwards” to evaluate the experimental viscosity functions using the measured poloidal rotation velocities as input. Since the deuterium poloidal velocity cannot be measured, we resort to the same type of stratagem used previously with the toroidal velocities by defining an effective viscosity function f_{eff} for both (all) ion species and combine Eqs. (22) in order to eliminate the unknown deuterium rotation velocity and obtain (for two ion species) a quadratic equation for f_{eff} ,

$$\begin{aligned}
& \left[\nu_{jk} + \nu_{\text{atom},j} + \frac{q u_{\text{th},j} f_{\text{eff}}}{R} \right] \\
& \times \left[\frac{e_k \nu_{rk} B_\phi}{m_k \nu_{kj}} + \left(1 + \frac{\nu_{\text{atom},k}}{\nu_{kj}} + \frac{q u_{\text{th},k} f_{\text{eff}}}{\nu_{kj} R} \right) \nu_{\theta k}^{\text{exp}} \right] - \nu_{jk} \nu_{\theta k}^{\text{exp}} \\
& = -\frac{e_j \nu_{rj} B_\phi}{m_j}, \quad (23)
\end{aligned}$$

which may be solved for f_{eff} by making use of the measured carbon impurity velocity $\nu_{\theta k}^{\text{exp}}$.

Once the f_{eff} is determined, it may be used, together with the measured carbon velocity $\nu_{\theta k}^{\text{exp}}$, to evaluate the “experimental” deuterium velocity from Eq. (22) for deuterium,

$$\nu_{\theta j} = \frac{\nu_{jk} \nu_{\theta k}^{\text{exp}} - e_j \nu_{rj} B_\phi / m_j}{\nu_{jk} + \nu_{\text{atom},j} + q u_{\text{th},j} f_{\text{eff}} / R}. \quad (24)$$

This same type of procedure can be carried out using Eq. (18) instead of Eq. (22), with similar but more complicated results.

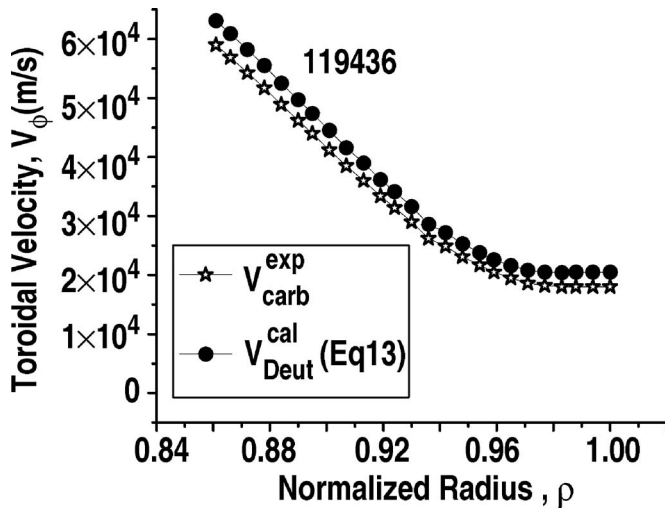


FIG. 3. Measured carbon toroidal rotation velocity and deuterium toroidal rotation velocity calculated using this measured velocity in Eq. (13), between ELMs in H-mode shot 119436.

VI. INTERPRETATION OF ROTATION MEASUREMENTS

A fit of the measured carbon toroidal rotation velocity $v_{\phi k}^{\text{exp}}$ shown in Fig. 2 for ELMing H-mode shot 119436 is plotted in Fig. 3. The difference between the deuterium and carbon toroidal velocities was calculated using Eq. (13) and added to this $v_{\phi k}^{\text{exp}}$ to obtain the deuterium velocity also shown in Fig. 3. The relatively small calculated difference between the velocities of the two species supports the validity of the underlying assumption of the perturbation analysis of Eqs. (11)–(14) (similar small differences were found also for the other two discharges considered in this paper). We note that similarly small differences were found recently between measured main He ion and carbon impurity ion toroidal rotation velocities in DIII-D¹⁵ (these results did not emphasize the edge), although rather larger differences were found earlier²² in the edge plasma. As discussed in Sec. IV, the relative toroidal rotation velocities of the two species depends on the interspecies collision frequency, the toroidal angular momentum transfer frequencies of the two species, and the beam momentum input to the two species; at least the first of which is quite sensitive to the plasma density and temperature.

The inferred angular momentum transfer rates for carbon (ν_{dk}) and deuterium ($\nu_{dj} = \nu_d^0$) calculated from Eqs. (14) and (12), respectively, are shown as C_{exp} and D_{exp} , respectively, for shot 119436 in Fig. 4. For comparison, the neoclassical gyroviscous momentum transfer frequency²⁵ for carbon and deuterium are shown also, as is the charge exchange plus elastic scattering plus ionization momentum transfer frequency, Datonic. These same quantities are shown for ELMing H-mode shot 98889 and ELM-free H-mode shot 118897 in Figs. 5 and 6, respectively. The neoclassical perpendicular angular momentum transfer frequency (not shown) is smaller by two orders of magnitude. Clearly, the neoclassical viscous and atomic physics phenomena are insufficient to account for the experimentally inferred angular momentum transfer rates over the edge pedestal, except perhaps just inside the separatrix (and the version of neoclassical gyroviscosity used for

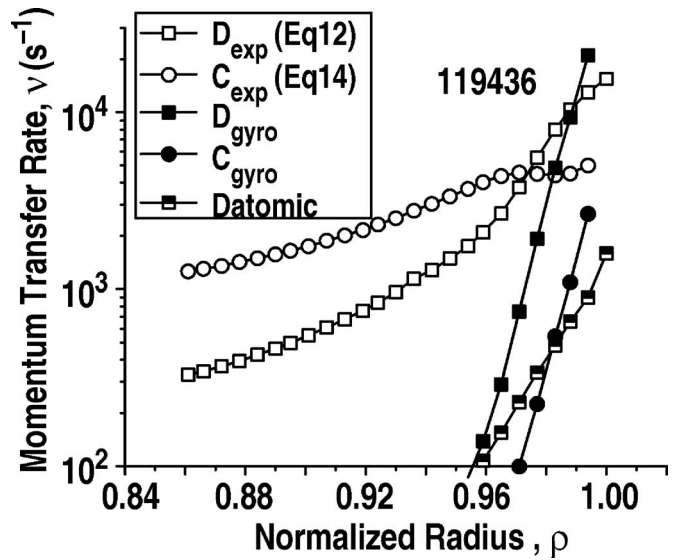


FIG. 4. Experimentally inferred toroidal angular momentum transfer frequency between ELMs in H-mode shot 119436.

the calculation may overpredict the transport rate in the steep gradient edge pedestal²⁶). It is interesting that the inferred momentum transport rates are larger (by about a factor of 5) in the ELMing shots than in the ELM-free H-mode shot.

A fit of the measured carbon poloidal rotation velocities from Figs. 1 and 2 and the values of the carbon and deuterium velocities calculated from Eqs. (18)–(21) and from Eqs. (22) are shown for the ELMing H-mode and the ELM-free H-mode shots 119436 and 118897 in Figs. 7 and 8, respectively. The Shaing–Sigmar parallel viscosity²³ $\eta_{0j} = n_j m_j v_{th,j} q R f_j(\nu_{jj}^*)$, with $f_j = \varepsilon^{-3/2} \nu_{jj}^* / (1 + \varepsilon^{-3/2} \nu_{jj}^*) (1 + \nu_{jj}^*)$, was used in the calculations. The experimental profiles are similar for the two shots, as are the calculated profiles. There is very little difference in Fig. 7 between the carbon poloidal velocity profiles calculated with Eqs. (18)–(21) (solid circles) and with Eq. (22) (half-solid circles). On the other

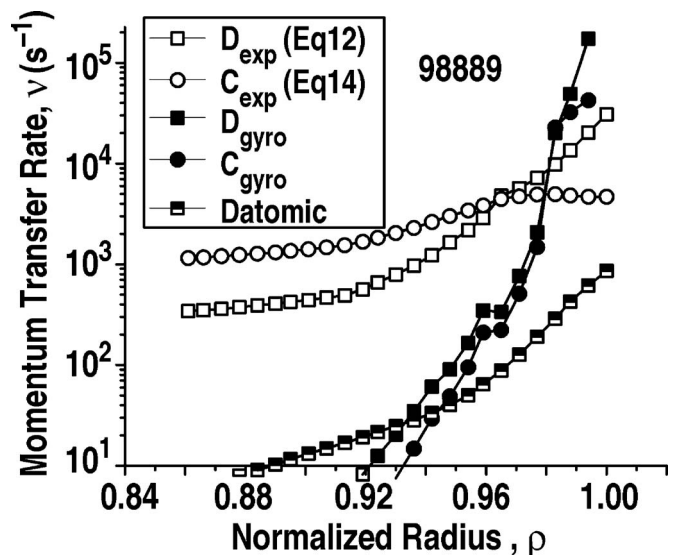


FIG. 5. Experimentally inferred toroidal angular momentum transfer frequency averaged over ELMs in H-mode shot 98889.

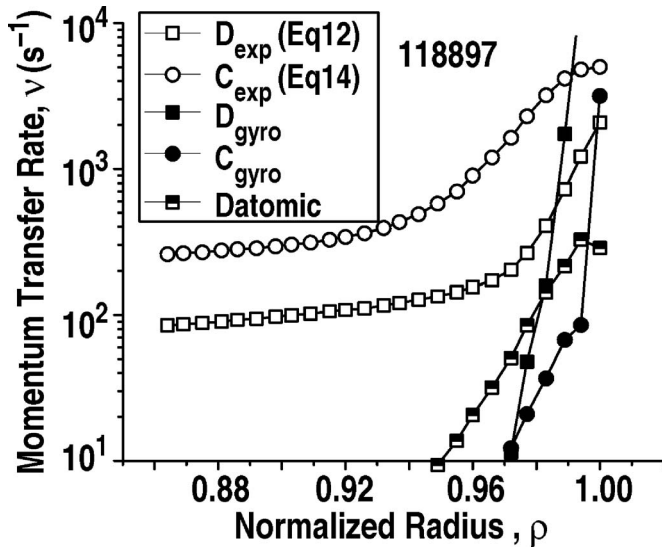


FIG. 6. Experimentally inferred toroidal angular momentum transfer frequency in ELM-free H-mode shot 118897.

hand, the deuterium velocity calculation with Eqs. (18)–(21) (solid squares falling almost directly under the open squares) is considerably different from the calculation with Eq. (22) (half-solid squares).

To provide some perspective, it is noted that the deuterium-carbon normalized collision frequency ν_{jk}^* increased with radius from 7.8×10^{-3} at $\rho=0.86$ to 6.2×10^{-2} at the separatrix, while the total atomic physics normalized collision frequency $\nu_{\text{atom}}^* = \nu_{\text{cs}}^* + \nu_{\text{el}}^* + \nu_{\text{ion}}^*$ varied from 1.7×10^{-4} to 8.7×10^{-2} over the same range for shot 119436.

The calculated and measured profiles are similar in magnitude, although they differ in sign at certain radial locations. [Note that the positive sense of the poloidal rotation is taken as the positive poloidal direction in a right-hand ($r-\theta-\phi$) with the positive ϕ direction aligned with the plasma current, which is down at the outboard midplane for these shots.] The deuterium velocity calculated from Eq. (18) using the measured carbon velocity (denoted as D_{exp}) is also shown in Fig.

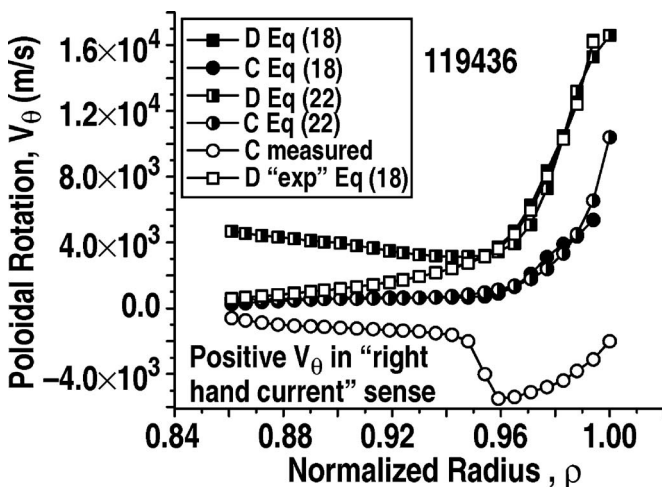


FIG. 7. Poloidal rotation velocities, measured and calculated, between ELMs in H-mode shot 119436.

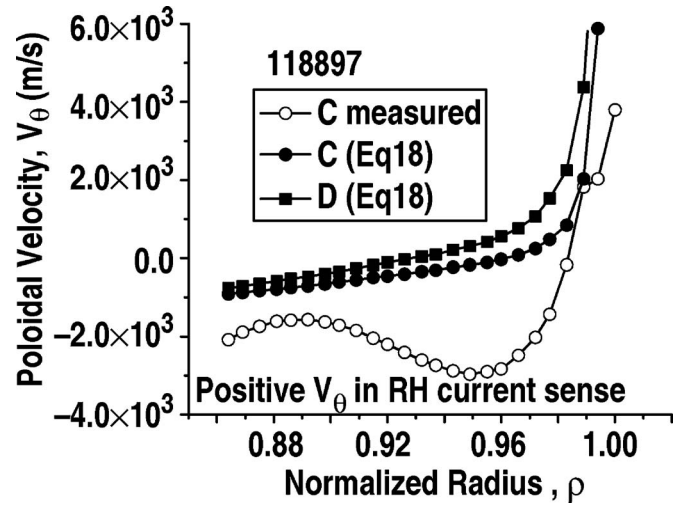


FIG. 8. Poloidal rotation velocities, measured and calculated, in ELM-free H-mode shot 118897.

7 [it falls almost exactly on top of the results calculated for deuterium when both species' velocities are calculated from Eqs. (18), making it difficult to see the latter].

The negative dip in the poloidal rotation velocity radial profile that is observed experimentally is not seen in the calculated profiles. Although the calculated carbon poloidal rotation velocities are in reasonably good agreement with measured values in the flattop region inward of the edge pedestal $\rho \leq 0.94$, the calculations clearly fail to predict the (negative) dips in poloidal velocity in the edge pedestal region.

An effective experimental parallel viscosity function f_{eff} was calculated from Eq. (23), using the measured carbon poloidal rotation velocity as input, and is shown in Fig. 9. Also shown are the neoclassical parallel velocity functions f_j for carbon and deuterium given by the Shaing-Sigmar expression²³ $f_j = \varepsilon^{-3/2} \nu_{jj}^* / (1 + \varepsilon^{-3/2} \nu_{jj}^*) (1 + \nu_{jj}^*)$. The experi-

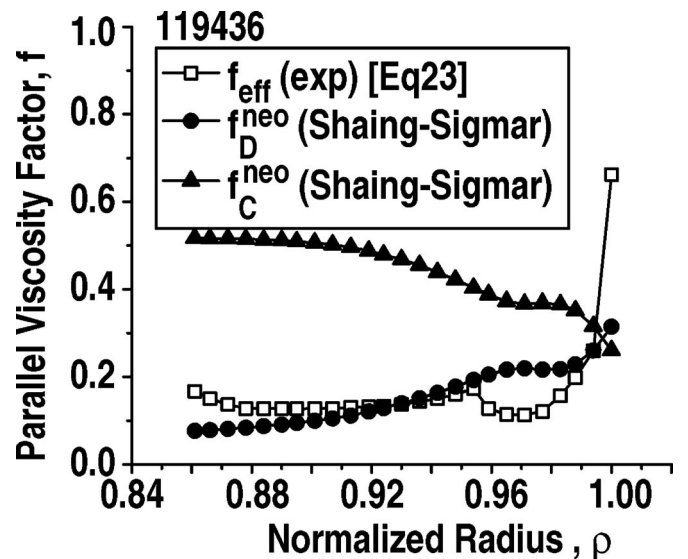


FIG. 9. Experimentally inferred and neoclassical calculated viscosity factor between ELMs in H-mode shot 119436.

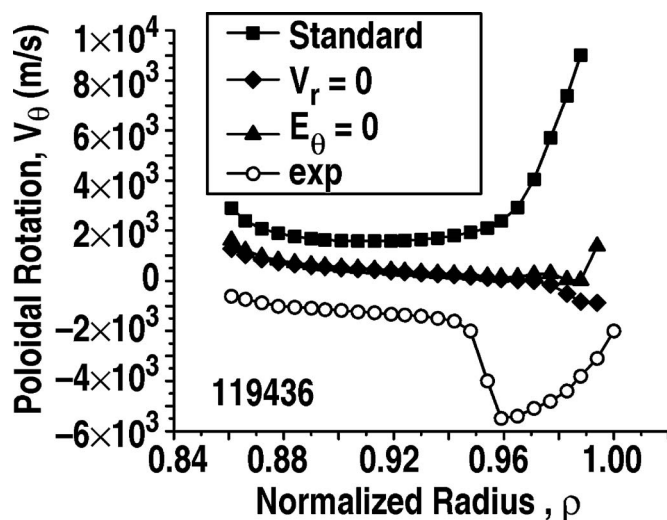


FIG. 10. Poloidal velocity calculation sensitivity studies. (Standard potential calculated by integrating $E_{\text{rad}}^{\text{exp}}$ from $\varphi_{\text{sep}} = -100$ eV, V_{rad} calculated by integrating continuity equation.)

mentally inferred f_{eff} is in good agreement with the neoclassical viscosity function f_j for deuterium for $\rho < 0.95$. The disagreement for $\rho > 0.95$ may well be due to Eq. (23), which is based on Eqs. (22) for the two species, attempting to account for the (negative) peaking in the velocity profile without containing the (unknown) term that causes it.

VII. SENSITIVITY CALCULATIONS

Since the radial particle velocity ($V \times B$ force) and the poloidal electric field are not usually retained in the development of equations for calculating the poloidal rotation velocities from poloidal momentum balance, it is of some interest to investigate the importance of these terms.

The radial particle velocity v_r enters the poloidal momentum balance via the $V \times B$ force term and is incorporated in Eqs. (18), (20), and (21) either explicitly or via the \hat{v}_r term defined in Eq. (19). In the “standard” calculation of poloidal rotation velocities presented in the previous figures, v_r was evaluated by integrating the continuity equation to obtain the $\Gamma_r = n v_r$ required at each radius to satisfy particle balance and then using the experimental value of n to obtain v_r . This quantity increased rapidly with radius just inside the separatrix due to a combination of an increasing ionization particle source, hence $\Gamma_r = n v_r$, and decreasing density. A calculation was performed setting the quantity $v_r = 0$. The carbon rotation velocity profile for the standard and the $v_r = 0$ calculations are compared in Fig. 10. Clearly the v_r term is important in the edge pedestal region.

Both the poloidal and radial electric fields are assumed electrostatic; thus, $E_r = -\partial\Phi/\partial r$ and $E_\theta = -\partial\Phi/r\partial\theta$. Representing $\Phi(r, \theta) = \Phi^0(r)(1 + \Phi^c \cos\theta + \Phi^s \sin\theta)$ leads to $E_\theta = -\Phi^0(r)[\Phi^s \cos\theta - \Phi^c \sin\theta]/r$. The electron poloidal momentum balance with only the E_θ and pressure gradients terms retained (or equivalently the Maxwell–Boltzmann distribution) then determines the relation $\tilde{\Phi}^{c/s} \equiv \Phi^{c/s}/\varepsilon$

$= n_e^{c/s}/\varepsilon(e\Phi^0/T_e)$, where the electron density variation is related to the ion density variations calculated from Eqs. (20) and (21) by charge neutrality.

In principle, the standard practice for determining the value of $\Phi^0(r_{\text{sep}})$ is to integrate the current continuity equation over the divertor and scrape-off layer, using sheath boundary conditions and taking into account drifts,²⁷ but such a calculation is beyond the scope of this paper. The FSA value of the potential was determined by integrating the experimental value of the radial electric field inward from the separatrix $\Phi^0(r) = \Phi^0(r_{\text{sep}}) + \int_{r_{\text{sep}}}^r E_r^{\text{exp}}(r') dr'$ using $\Phi^0(r_{\text{sep}}) = -100$ eV. The experimental radial electric field was negative at the separatrix, became more negative in the edge pedestal then decreased in magnitude and became positive in the flattop region. We note that it is the product $\Phi^0\Phi^{s,c}$ (i.e., the poloidal electric field) that enters the above equations and that $\tilde{\Phi}^{c/s} \equiv \Phi^{c/s}/\varepsilon = n_e^{c/s}/\varepsilon(e\Phi^0/T_e)$, so the product $\Phi^0\Phi^{s,c} \sim E_\theta$ is independent of Φ^0 .

To test the sensitivity of the poloidal rotation velocity calculation to the inclusion of the poloidal electric field, the calculation was repeated for $E_\theta = 0$. The calculated carbon poloidal velocity profile for $E_\theta = 0$ is also plotted in Fig. 10. Clearly, the inclusion of E_θ is important for the determination of the poloidal rotation velocity in the edge pedestal.

VIII. SUMMARY AND CONCLUSIONS

A methodology was presented for inferring experimental toroidal angular momentum transfer rates from measured toroidal rotation velocities in the edge pedestal. This methodology was applied to analyze transfer rates of toroidal angular momentum in the edge pedestal of three DIII-D H-mode shots. The inferred angular momentum transfer rates are larger than can be explained by atomic physics or neoclassical viscosity, which suggests the presence of other torque/momentum transport mechanisms (e.g., orbit scrape-off, turbulent).

Calculations of poloidal rotation velocities (based on poloidal momentum balance, using neoclassical parallel viscosity, and taking into account atomic physics) were compared with measured values of the carbon poloidal rotation velocities in the edge pedestal of three DIII-D shots. In the flattop region just inside the edge pedestal there was reasonable agreement between calculation and experiment. However, the calculation failed to reproduce the measured structure in the poloidal velocity in the edge pedestal, indicating the presence of some important momentum transport or torque input mechanism in the edge pedestal region that was not accounted for in the calculation.

A novel feature of the poloidal rotation calculation was retention in the poloidal momentum balance of radial particle velocity and poloidal electric field terms usually neglected. Both of these terms were demonstrated to be important in the edge pedestal.

ACKNOWLEDGMENTS

This work was supported by the U.S. Department of Energy Grant No. DE-FG02-00-ER54538 with the Georgia Tech Research Corporation and by the U.S. Department of

Energy Contract No. DE-AC03-99ER54463 with General Atomics Co. The authors are grateful to members of the DIII-D Team who took part in measuring and reducing the data used in this paper. The first author appreciates the hospitality provided by General Atomics during part of this work.

APPENDIX: NEOCLASSICAL PARALLEL VISCOUS FORCE REPRESENTATION

Stacey and Sigmar²⁵ generalized Braginskii's flow stress tensor results²⁸ to toroidal geometry and replaced the Braginskii collisional viscosity coefficient with the Shaing–Sigmar coefficient given above to obtain for the flow contribution to the parallel viscous force:

$$\langle \mathbf{B} \cdot \nabla \cdot \Pi_{\parallel}^i \rangle^{\text{St-S}} = \frac{3}{2} \left\langle \eta_{0j} A_{0j}^{\theta} \frac{\partial B_{\theta}}{\partial \ell_{\theta}} \right\rangle \bar{v}_{\theta j} + \frac{3}{2} \left\langle \eta_{0j} A_{0j}^{\phi} \frac{\partial B_{\theta}}{\partial \ell_{\theta}} \right\rangle \bar{v}_{\phi j}, \quad (\text{A1})$$

where

$$A_{0j}^{\theta} = \frac{2 \left\{ -\frac{1}{3} \left(\frac{\partial v_{\theta j}}{\partial l_{\theta}} \right) + \left[\left(\frac{1}{R} \right) \frac{\partial R}{\partial l_{\theta}} + \frac{1}{3} \left(\frac{1}{B_{\theta}} \right) \frac{\partial B_{\theta}}{\partial l_{\theta}} \right] v_{\theta j} \right\}}{\bar{v}_{\theta j}} \quad (\text{A2a})$$

and

$$A_{0j}^{\phi} = \frac{2 f_p R \frac{\partial (v_{\phi j} / R)}{\partial l_{\theta}}}{\bar{v}_{\phi j}}. \quad (\text{A2b})$$

This form introduced the contribution of poloidal asymmetries in both the poloidal and toroidal velocities (as well as the density) into the parallel viscous force. The overbar on the velocity in Eqs. (A1), (A2a), and (A2b) distinguishes the FSA quantity from the poloidally varying quantity. The Stacey–Sigmar form of the parallel viscous force has been extended²⁹ to take into account neoclassical heat flux contributions

$$\langle \mathbf{B} \cdot \nabla \cdot \Pi_{\parallel}^i \rangle^{\text{St-S}}_{\text{ext}} = \frac{3}{2} \left\langle \eta_{0j} A_{0j}^{\theta} \frac{\partial B_{\theta}}{\partial \ell_{\theta}} \right\rangle \left[\bar{v}_{\theta j} + \frac{B_{\phi} K^j T_j L_{Tj}^{-1}}{e_j B^2} \right] + \frac{3}{2} \left\langle \eta_{0j} A_{0j}^{\phi} \frac{\partial B_{\theta}}{\partial \ell_{\theta}} \right\rangle \bar{v}_{\phi j}. \quad (\text{A3})$$

- ¹R. J. Groebner and T. H. Osborne, Phys. Plasmas **5**, 1800 (1998).
- ²A. E. Hubbard, R. L. Boivin, R. S. Granetz *et al.*, Phys. Plasmas **5**, 1744 (1998).
- ³W. Suttrop, O. Gruber, B. Kurzan *et al.*, Plasma Phys. Controlled Fusion **42**, A97 (2000).
- ⁴T. H. Osborne, J. R. Ferron, R. J. Groebner *et al.*, Plasma Phys. Controlled Fusion **42**, A175 (2000).
- ⁵M. Kotschenreuther, W. Dorland, Q. P. Liu *et al.*, *Proceedings of the 16th Conference on Plasma Physics Controlled Fusion Research, Montreal*, 1996 (IAEA, Vienna, 1997), Vol. 2, p 371.
- ⁶J. E. Kinsey, R. E. Waltz, and D. P. Schissel, Proceedings of the 24th European Physical Society, Berchtesgarden, 1997, Vol. III, p 1081; Plasma Phys. Controlled Fusion **42**, A97 (2000).
- ⁷W. M. Stacey, Phys. Plasmas **11**, 4295 (2004).
- ⁸W. M. Stacey and R. J. Groebner, Phys. Plasmas **13**, 012513 (2006).
- ⁹J. Luxon, Nucl. Fusion **42**, 614 (2002).
- ¹⁰Y. Koide, T. Takizuka, S. Takeji *et al.*, Plasma Phys. Controlled Fusion **38**, 1011 (1996).
- ¹¹D. R. Ernst, M. G. Bell, R. E. Bell *et al.*, Phys. Plasmas **5**, 665 (1998).
- ¹²P. Gohil, K. H. Burrell, R. J. Groebner *et al.*, *Proceedings of the 14th Symposium on Fusion Engineering, San Diego*, 1991 (Institute of Electrical and Electronics Engineers, New York, 1992), Vol. 2, p. 1199.
- ¹³W. M. Stacey and R. J. Groebner, Phys. Plasmas **14**, 012501 (2007).
- ¹⁴W. M. Stacey and R. J. Groebner, Phys. Plasmas **14**, 122504 (2007).
- ¹⁵L. R. Baylor, K. H. Burrell, R. J. Groebner *et al.*, Phys. Plasmas **11**, 3100 (2004).
- ¹⁶P. Gohil, K. H. Burrell, R. J. Groebner *et al.*, Rev. Sci. Instrum. **70**, 878 (1999).
- ¹⁷W. M. Solomon, K. H. Burrell, R. Andre *et al.*, Phys. Plasmas **13**, 056116 (2006).
- ¹⁸W. M. Stacey, Phys. Plasmas **5**, 1015 (1998); **8**, 3673 (2001); Nucl. Fusion **40**, 678 (2000).
- ¹⁹W. M. Stacey, R. W. Johnson, and J. Mandrekas, Phys. Plasmas **13**, 062508 (2006).
- ²⁰J. E. Rice, E. S. Marmor, P. T. Bonoli *et al.*, Fusion Sci. Technol. **51**, 288 (2007).
- ²¹W. M. Solomon, Princeton Plasma Physics Lab, personal communication (2007).
- ²²J. Kim, K. H. Burrell, P. Gohil *et al.*, Phys. Rev. Lett. **72**, 2199 (1994).
- ²³W. M. Stacey, A. W. Bailey, D. J. Sigmar, and K. C. Shaing, Nucl. Fusion **25**, 463 (1985).
- ²⁴W. M. Stacey, Phys. Plasmas **9**, 3874 (2002).
- ²⁵W. M. Stacey and D. J. Sigmar, Phys. Fluids **28**, 2800 (1985).
- ²⁶H. A. Claassen, H. Gerhauser, and A. Rogister, Phys. Plasmas **7**, 3699 (2000).
- ²⁷T. D. Rognlien, D. D. Ryutov, N. Mattor, and G. D. Porter, Phys. Plasmas **6**, 1851 (1999).
- ²⁸S. I. Braginskii, Rev. Plasma Phys. **1**, 205 (1965).
- ²⁹W. M. Stacey, Phys. Plasmas **15**, 012501 (2008).